

# Creation of Two-Dimensional Electron Gas at the Heterointerface of CaZrO<sub>3</sub>/KTO with Tunable Rashba Spin–Orbit Coupling

Shaojin Qi, Jiexing Liang, Guimei Shi, Yulin Gan, Yuansha Chen,\* Yunzhong Chen,\* and Jirong Sun\*

Cite This: *ACS Appl. Electron. Mater.* 2024, 6, 8404–8412

Read Online

ACCESS |



Metrics &amp; More



Article Recommendations



Supporting Information

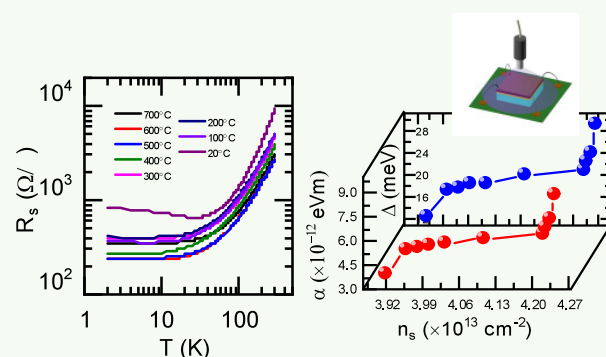
**ABSTRACT:** Compared to SrTiO<sub>3</sub>-based 3d two-dimensional electron gases (2DEGs), KTO-based 5d 2DEGs have much more exceptional physical properties, such as a higher Curie temperature of spin-polarized 2DEG, higher  $T_c$  for the 2DEG at superconducting state, and larger spin–orbit coupling. Herein, the CaZrO<sub>3</sub> (CZO) films were deposited on KTO (001) substrates at the deposition temperature varied from 700 °C to room temperature, and the conductive CZO/KTO interface was obtained at all deposition temperatures. The conductivity of the CZO/KTO heterointerface exhibits critical dependence on the film thickness, where the critical thickness for conduction increases from 3.2 to 6 nm when decreasing the deposition temperature from 700 °C to room temperature. Moreover, the electric properties of the heterointerface grown at room temperature can be modulated strongly by the light illumination. The strength of the spin–orbit coupling exhibits large relative variation with the carrier density. Under the light illumination, the strength of the spin–orbit coupling increases from  $\sim 3.9 \times 10^{-12}$  eV m to the maximum of  $\sim 9 \times 10^{-12}$  eV m, with the maximal change of the carrier density of only  $3 \times 10^{12}$  cm<sup>-2</sup>. The present work demonstrates an effective tuning of the special 5d-electron-based 2DEGs by light illumination, showing a feasible way for advanced optoelectronic device application.

**KEYWORDS:** CaZrO<sub>3</sub>/KTO heterostructure, deposition temperature, conductive interface, light illumination, spin–orbit coupling

## 1. INTRODUCTION

The prime example of highly mobile two-dimensional electron gases (2DEGs) at the surfaces or interfaces of complex oxides is the LaAlO<sub>3</sub>/SrTiO<sub>3</sub> (LAO/STO) interface, which has been extensively studied in the past decade.<sup>1</sup> It possesses diverse and exotic properties, such as two-dimensional superconductivity,<sup>2</sup> magnetism,<sup>3–5</sup> Rashba effect<sup>6–9</sup> and efficient spin-to-charge conversion,<sup>10,11</sup> demonstrating the importance of the oxide 2DEGs for both fundamental and applied research. In addition to LAO/STO, the anticipation of 2DEGs at the interface of other special oxides has aroused extensive investigations. Various heterostructures were synthesized to produce the conductive interface as long as STO substrate was involved, such as LaTiO<sub>3</sub>/STO,<sup>12</sup> NdGaO<sub>3</sub>/STO,<sup>13,14</sup>  $\gamma$ -Al<sub>2</sub>O<sub>3</sub>/STO<sup>15,16</sup> and CaZrO<sub>3</sub> (CZO)/STO.<sup>17,18</sup> The origin of the interfacial 2DEGs, i.e., a conductive layer at the surface or interface of the substrate, originates mainly from the polarity-discontinuity-induced electronic reconstruction<sup>19,20</sup> or interfacial redox reactions.<sup>21–23</sup>

Apart from STO-based 2DEGs where the electron comes from the 3d  $t_{2g}$  orbitals, KTO as a kind of substrate material can also be used to induce 2DEGs. Although KTO shares many properties with STO such as high permittivity<sup>24</sup> and quantum paraelectricity,<sup>25</sup> it is different from STO as a 5d



transition metal oxide with heavy elements and stronger atomic spin–orbit coupling. Compared to STO-based 2DEGs, the well spin-polarized KTO-based 2DEGs with stronger ferromagnetic state and higher Curie temperature was found in the EuO/KTO heterostructure.<sup>26</sup> The superconductivity property was also revealed in KTO-based 2DEGs recently,<sup>27–29</sup> which can be tuned by the gate electric field.<sup>30</sup> The critical temperature  $T_c$  is up to 2 K for a (111) interface, much higher than that of STO-based 2DEGs. For the KTO-based 2DEGs, the conductive electrons are confined in the quantum well at the interface or surface. The broken structural inversion symmetry generates a Rashba spin–orbit coupling. KTO-based 2DEGs, as a type of 5d-electron 2DEGs, possesses stronger spin–orbit coupling, which can be modulated by light and gate voltage.<sup>31,32</sup> The strength of spin spin–orbit coupling exhibits a dome feature as a function of carrier density, i.e., band filling. The spin-splitting energy originated from spin–orbit coupling

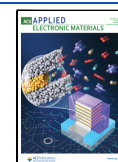
transition metal oxide with heavy elements and stronger atomic spin–orbit coupling. Compared to STO-based 2DEGs, the well spin-polarized KTO-based 2DEGs with stronger ferromagnetic state and higher Curie temperature was found in the EuO/KTO heterostructure.<sup>26</sup> The superconductivity property was also revealed in KTO-based 2DEGs recently,<sup>27–29</sup> which can be tuned by the gate electric field.<sup>30</sup> The critical temperature  $T_c$  is up to 2 K for a (111) interface, much higher than that of STO-based 2DEGs. For the KTO-based 2DEGs, the conductive electrons are confined in the quantum well at the interface or surface. The broken structural inversion symmetry generates a Rashba spin–orbit coupling. KTO-based 2DEGs, as a type of 5d-electron 2DEGs, possesses stronger spin–orbit coupling, which can be modulated by light and gate voltage.<sup>31,32</sup> The strength of spin spin–orbit coupling exhibits a dome feature as a function of carrier density, i.e., band filling. The spin-splitting energy originated from spin–orbit coupling

**Received:** September 11, 2024

**Revised:** October 23, 2024

**Accepted:** October 31, 2024

**Published:** November 11, 2024



is at the maximum of 30 meV larger than that of STO-based 3d 2DEGs ( $\Delta \approx 1\text{--}10$  meV).<sup>6,31</sup>

In short, 5d oxide-based 2DEGs are an ideal platform to research electronic correlation and effects of spin–orbit coupling. Zhang et al.<sup>33,34</sup> fabricated the amorphous LaAlO<sub>3</sub>/KTaO<sub>3</sub> heterostructures at different growth temperatures. The carrier density and mobility strongly depend on the film growth temperature. Because of the large lattice mismatch of 2.67% in the LAO/KTO system, the LAO overlayer grown on the KTO substrate is amorphous. K. Zou et al.<sup>35</sup> and Y. Zou et al.<sup>36</sup> deposited LaTiO<sub>3</sub> and EuTiO<sub>3</sub> films on the KTaO<sub>3</sub> substrates, and the epitaxy growth of the films was achieved. The 2DEGs at the heterointerface exhibit anomalous Hall resistance and Rashba spin–orbit coupling. Besides, the conductive interface can also be achieved at STO/KTO,<sup>37</sup> LaVO<sub>3</sub>/KTaO<sub>3</sub>,<sup>38,39</sup> LaCrO<sub>3</sub>/KTaO<sub>3</sub><sup>40</sup> and  $\gamma$ -Al<sub>2</sub>O<sub>3</sub>/KTaO<sub>3</sub><sup>41</sup> heterostructures. All of these results indicate that the formations of 2DEGs at the 5d KTO-based heterointerfaces are feasible. The CZO/KTO conductive heterointerface,<sup>42</sup> which was researched at 2024, shows nonreciprocal magneto-resistance transport due to the Rashba spin–orbit coupling tuned by light illumination. It is of great significance for the fabrication of spintronic devices. Herein, we systematically prepared a series of epitaxial KTO heterostructures by growing CZO ( $a = 4.012$  Å) films on the KTO substrates at different deposition temperatures,<sup>43</sup> where there is a good lattice match with KTO ( $a = 3.989$  Å) with a lattice mismatch of only 0.58%, far less than the mismatch of 2.67% in the LAO/KTO system, leading to the better epitaxial growth of the CZO film. The metallic interface was obtained in the CZO/KTO heterostructure, which shows the strong signature of Rashba spin–orbit coupling tunable by the light illumination. An effective tuning of carrier density and thus the conductance can be achieved by light irradiation. Moreover, the strength of the spin–orbit coupling exhibits a large relative variation with the carrier density under the light. This epitaxial CZO/KTO interface can open up the achievement of a conductive heterointerface system and electronic devices.

## 2. EXPERIMENTAL SECTION

The conductive interfaces were fabricated by growing CZO films with different thicknesses on (001)-oriented KTaO<sub>3</sub> single-crystal substrates using the technique of pulsed laser deposition (PLD) with a ceramic CZO target. The fluence of the laser pulse was 1.5 J/cm<sup>2</sup>, and the repetition rate was 1 Hz (KrF excimer laser, wavelength = 248 nm). During the deposition, the growth temperature ( $T_s$ ) was varied at  $T_s = 700$  °C, 600 °C, 500 °C, 400 °C, 300 °C, 200 °C, 100 °C and room temperature 20 °C. The pressure of the chamber of the PLD devices was fixed on  $5 \times 10^{-7}$  mbar. After the deposition of the films, the samples were furnace-cooled to room temperature without changing the pressure of the chamber. The diffraction patterns of the samples before and after the CZO overlayer were obtained by reflected high-energy electron diffraction (RHEED) *in situ*. The epitaxial growth of the CZO film was also confirmed by X-ray diffraction (XRD) measurements.

Resistance measurements were performed by a Quantum design physical property measurement system (PPMS) in the temperature interval from 2 to 300 K. The van der Pauw geometry was adopted for electric measurements. Ultrasonic wire bonding (Al wire of 20  $\mu$ m diameter) was used for electrode contact. The applied current for resistance measurements was 10  $\mu$ A. To investigate the effect of photo excitation, a laser beam ( $\lambda = 405$  nm) was introduced into PPMS by an optical fiber.

## 3. RESULTS AND DISCUSSION

Figure 1a illustrates the heterostructure of the CZO epitaxially grown on the perovskite KTO substrate with the TaO<sub>2</sub>

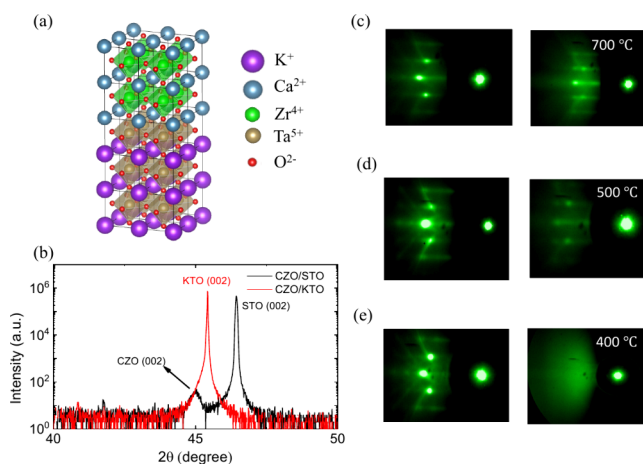


**Figure 1.** (a) The crystal structure of the CZO/KTO heterostructure with the TaO<sub>2</sub> termination. (b) X-ray diffraction patterns of the CZO/KTO and CZO/STO heterostructures prepared at 700 °C. (c)–(e) The RHEED patterns before (left) and after (right) the deposition of the CZO/KTO heterostructures with the deposition temperature of 700, 500 and 400 °C, respectively.

termination plane as an example. The mean roughness of the KTO substrate surface is less than 0.4 nm (Supporting Information, Figure S1). The CZO films also exhibit a low-roughness surface as shown in Figure S2.

The thickness of the CZO layer can be obtained by the X-ray reflection (XRR) measurement (Figure S3). Figure 1b shows the comparison of the XRD patterns for the CZO/KTO and CZO/STO heterostructures prepared at 700 °C. The XRD patterns of CZO/KTO and CZO/STO heterostructures prepared at different temperatures are also presented in the Supporting Information, Figure S4. Because the lattice constant of the CZO film is close to that of the KTO substrate, their (002) diffraction peaks coincide approximately, and we mainly focus on the CZO/STO samples. The XRD patterns of CZO/STO heterostructures prepared at 700 °C, 500 °C and 400 °C are presented in the Supporting Information, Figure S4b. As the deposition temperature goes down to 400 °C, the diffraction peaks of the CZO film do not exist, indicating the CZO film is not at the crystalline state at the low growth temperature.

To demonstrate epitaxial growth of the CZO film on the KTO substrate, reflected high-energy electron diffraction (RHEED) characterization of the sample prepared at varied temperatures was made. As shown in Figure 1c–e, clear streaky RHEED patterns of the epitaxial CZO films are observed for the deposition temperatures 500–700 °C, which indicates the epitaxial growth of the CZO film. The RHEED patterns become indistinct when the deposition temperature is lower than 500 °C. Below 400 °C, no diffraction patterns are visible, demonstrating the disordered or amorphous state of the CZO film at low temperatures, which is consistent with the XRD of the CZO/STO heterostructure.

A metallic interface is formed at the CZO/KTO heterointerface for all the growth temperatures (deposition temperatures)  $T_s$ , and its conductivity is found to depend critically on both  $T_s$  and CZO film thickness,  $t$ . We obtained the conductive

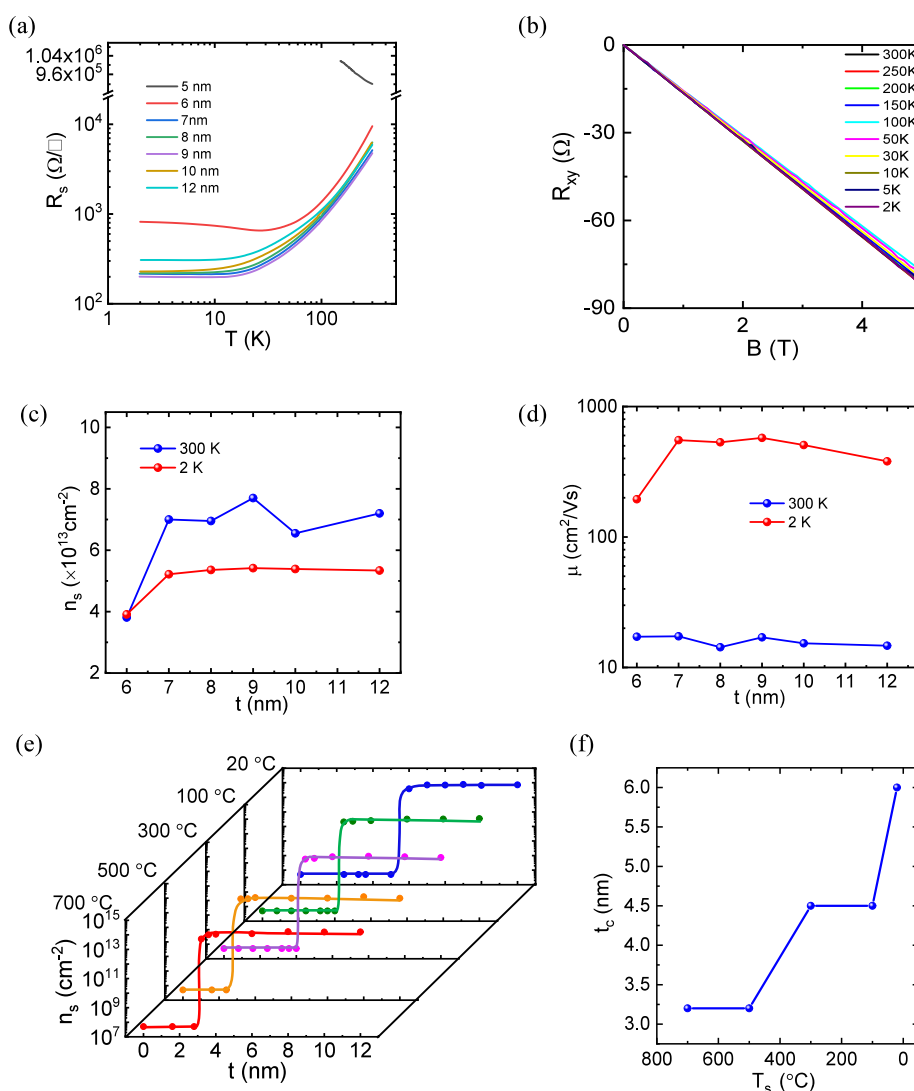


**Figure 2.** (a)  $R_s$ – $T$  curves of the samples prepared at room temperature with different CZO thicknesses. (b) Hall resistance of 6 nm CZO/KTO heterostructure grown at room temperature. (c) The carrier density at 2 and 300 K as a function of CZO thickness. (d) The mobility at 2 and 300 K as a function of CZO thickness. (e) The carrier density at 300 K as a function of thickness of the CZO overlayer for the conducting CZO/KTO interfaces grown at different temperatures. (f) The relationship between the critical thickness of the CZO layer and deposition temperature.

heterointerface at the deposition temperature of room temperature. Figure 2a is the  $R_s$ – $T$  curves of the samples prepared at room temperature with different CZO thicknesses. For  $t = 5$  nm, the resistance of the sample is on the order of magnitude of  $10^6 \Omega/\square$  and shows the upward trend with the temperature decreasing. The interface of the heterostructure is insulating. As the thickness of CZO layer is more than 6 nm (the critical value), the samples exhibit metallicity. All the Hall resistance curves display a linear dependence of magnetic field (Figure 2b), indicating that only one species of carrier has identical mobility. The  $n_s$  is dominated by electrons and is extracted by Hall effect measurement by  $n_s = 1/|e|lR_H$  with the elementary charge  $e$  and the Hall coefficient  $R_H = dR_{xy}/dB$ . The carrier density at 300 and 2 K as a function of CZO thickness is presented in Figure 2c. When the thickness of the CZO layer is at the critical value for the conduction, the carrier density is  $\sim 3.9 \times 10^{13} \text{ cm}^{-2}$ , obviously lower than other samples. As the CZO layer thickness is larger than the critical value, the carrier density grows higher and values are close to each other. The carrier mobility expressed as  $\mu = 1/R_H n_s l$  is

the order of magnitude of  $10^2 \text{ cm}^2/(\text{V s})$ , practically independent of the overlayer thickness (Figure 2d). The electric transport of the samples prepared at 700 °C with a similar dependence on the CZO layer thickness is presented in the Supporting Information, Figure S5.

Figure 2e summarizes the thickness dependent sheet carrier density ( $n_s$ ) at 300 K of CZO/KTO grown at different  $T_s$  values. All samples undergo a sharp insulator–metal transition when the thickness of the CZO overlayer exceeds the critical thickness,  $t_c$ . With the decreasing  $T_s$  from 700 °C to room temperature, the critical thickness increases from 3.2 to 6 nm (shown in Figure 2f), which is consistent with the redox reaction scenario at interfaces where lowering the substrate temperature will significantly reduce the oxygen diffusion coefficient based on the thermally activated process of oxygen diffusion as observed in the  $\gamma\text{-Al}_2\text{O}_3/\text{STO}$  heterostructures.<sup>16</sup> Specifically, during the deposition of the CZO film, the KTO substrate oxidizes the CZO overlayer, leading to the generation of oxygen vacancies in proximity to the KTO surface. For the growth condition of low oxygen pressure, oxygen diffusion is

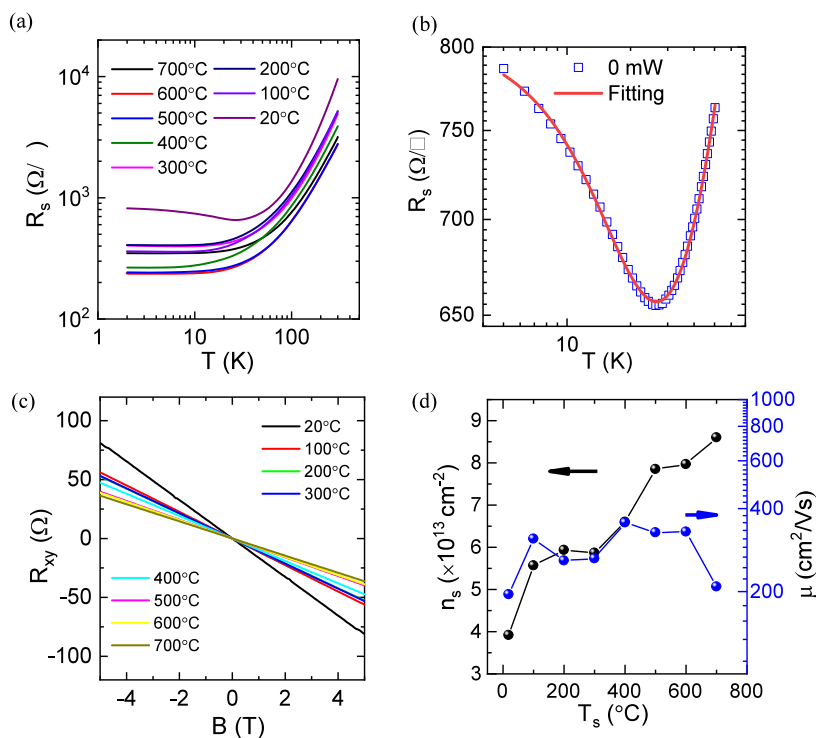


**Figure 3.** (a)  $R_s$ - $T$  curves of the 6 nm CZO/KTO heterostructures grown from room temperature to 700 °C. (b) The result of the  $R_s$ - $T$  curve fitting with light illumination. (c) The Hall resistance at 2 K as a function of magnetic field  $B$  for different  $T_s$  values. (d) The carrier density and mobility at 2 K as a function of the deposition temperature  $T_s$ .

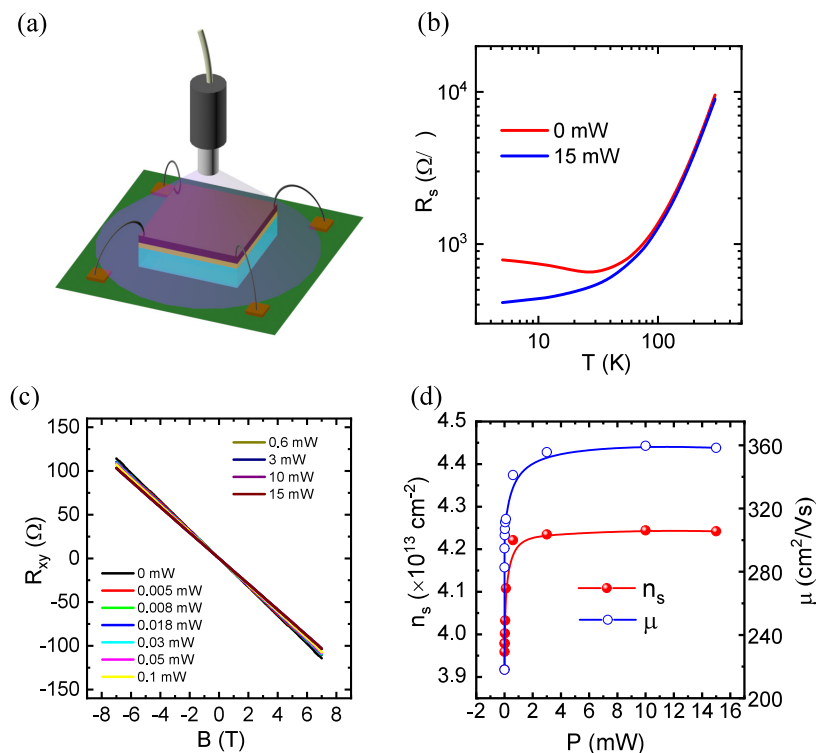


**Figure 4.** (a) The sketch of the experiment setup for the sample illuminated by the light. (b) The  $R_s$ - $T$  curves at the light power of 0 and 15 mW. (c) Hall resistance curves with different light powers. (d) The carrier density and the mobility as a function of the light power.

the major factor in the formation of oxygen vacancies, leading to the creation of the conductive carriers. When the CZO overlayer is thin, the content of the doped electron is low and the interfacial layer remains insulating, although the local

conducting regions might appear. When the thickness of the CZO layer is larger than a critical level, a percolation of the separately conducting regions takes place, resulting in metallic behavior.

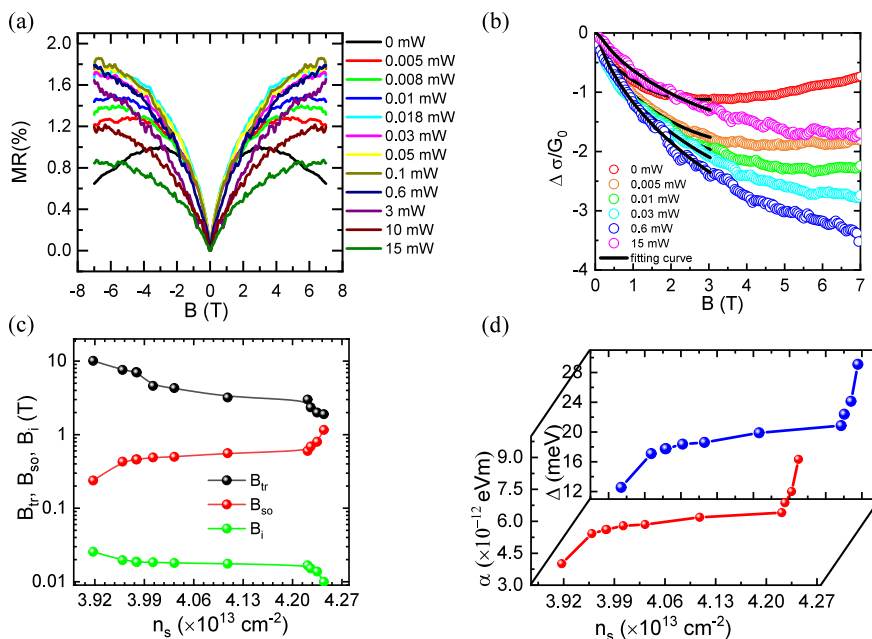


**Figure 5.** (a) The magnetoresistance curves with different light powers. (b) A demonstration of the magnetoresistance curves fitting with the eq 2. (c)  $B_{tr}$ ,  $B_i$  and  $B_{so}$  as a function of the carrier density. (d) The strength of spin–orbit coupling  $\alpha$  and spin-splitting energy  $\Delta$  as a function of carrier density.

To further investigate the interfacial electric transport properties, we measured the sheet resistance as a function of temperature for the CZO/KTO heterostructures ( $t = 6$  nm) grown at different  $T_s$  values, as presented in Figure 3a. The  $R_s$ – $T$  curves suggest that all of the heterointerfaces grown from 700 °C to room temperature are metallic, and the sheet resistance of 2 K ranges from  $\sim 200$  to  $\sim 1800$   $\Omega/\square$ . Significantly, the resistance exhibits upturn with saturation at the low temperature of  $T < 100$  K, indicating the appearance of the Kondo effect. The Kondo effect originated from the localized magnetic moment could come from the electronic reconstruction near  $Ta^{4+}$  accompanied by the formation of oxygen vacancies. The localized magnetic moment scatters and couples antiferromagnetically with the itinerant electrons.<sup>3</sup> As the temperature is lowered, the spin of the impurity ions is screened by the spin of the conduction electrons. And below a characteristic temperature (Kondo temperature,  $T_K$ ), the resistance gradually saturates. As shown by the red solid line in Figure 3b, the  $R_s$ – $T$  dependence below 100 K can be well reproduced by the standard formula,<sup>44</sup>

$$R_s = R_0 + aT^q + C \left( 1 - \frac{\ln(T/T_k)}{\sqrt{(\ln(T/T_k))^2 + \pi^2 S(S+1)}} \right) \quad (1)$$

where  $T_k$  is the effective Kondo temperature and  $S$  is the effective spin of the magnetic scattering centers. The  $R_0$  is the residual resistance due to sample disorder. The second term of this equation,  $aT^q$ , describes the transport behavior determined by electron–electron and electron–phonon interactions. The fitting parameters are  $T_k = 20.20$  K and  $S = 0.13$ , which are comparable to those of conductive interface at amorphous  $LaAlO_3/KTaO_3$  heterostructure.<sup>34</sup>

The Hall resistance for CZO/KTO heterostructures ( $t = 6$  nm) deposited at different temperatures and the corresponding

carrier density and mobility at 2 K are compared in Figure 3c and Figure 3d. With the deposition temperature becoming lower, the carrier density at low temperature decreases from  $8.6 \times 10^{13}$   $cm^{-2}$  for  $T_s = 700$  °C to  $3.9 \times 10^{13}$   $cm^{-2}$  for  $T_s = 20$  °C. This result could be attributed to the fact that the reduction of the  $T_s$  restricts the diffusion of oxygen atom from the KTO substrate to CZO overlayer and ambient atmosphere, leading to the decreasing of oxygen vacancies. The carrier mobility is on the same order around 200–400  $cm^2/(V s)$  at 2 K for all the investigated  $T_s$ .

The sample with lower carrier density is more sensitive to external stimuli, such as light illumination or electric field. During this experiment, a 6 nm CZO/KTO sample prepared at room temperature, which shows the lowest carrier density, was tuned by light illumination. The samples were illuminated by a beam of violet laser ( $\lambda = 405$  nm), which is presented in Figure 4a. Though the photon energy of the light ( $\sim 3$  eV) in this experiment is lower than the KTO band gap ( $\sim 3.5$  eV), the oxygen vacancies in KTO can generate normally electronic states at the conduction-band edge, decreasing the band gap.<sup>45</sup> So only the electrons confined in the KTO in-gap states can be excited to the conduction band. The photogenerated electrons could be trapped in the interfacial potential well, leading to the increase of the carrier density and thus conductance. Figure 4b shows the  $R_s$ – $T$  curves upon cooling for the CZO/KTO heterostructure with and without light exposure. The light illumination enhances the conductivity of the heterointerface. The sheet resistivity at 5 K is modulated from  $\sim 780$  to  $\sim 410$   $\Omega/\square$ . Upon the light illumination, the Kondo effect is strongly suppressed and the  $R_s$ – $T$  curve exhibits a perfect metallic behavior. Perhaps the electron–electron interaction and the coherence between the localized spin centers are minimized by the light illumination, so the Kondo effect is suppressed.<sup>46</sup>

As shown in Figure 4c, the Hall resistance changes linearly with the magnetic field over the whole range of the light power (0–15 mW). The slope of the Hall resistance decreases as the light power becomes larger, which corresponds to the variation

of the carrier density. The calculated carrier density and mobility as a function of the light power are presented in Figure 4d. As the light power increases, the carrier density increases accordingly, from the initial value of  $3.9 \times 10^{13} \text{ cm}^{-2}$  to the saturated value  $4.2 \times 10^{13} \text{ cm}^{-2}$  at  $P = 15 \text{ mW}$ . The carrier mobility also gets the maximum of  $300 \text{ cm}^2/(\text{V s})$  at the light power of  $15 \text{ mW}$ .

The magnetoresistance ( $\text{MR} = [R(B) - R(0)]/R(0)$ ) at low temperatures can also be modulated by light illumination with different light powers. Figure 5a shows the magnetic field dependence of MR at  $T = 5 \text{ K}$  under different light powers. The magnetic field is from  $-7$  to  $+7 \text{ T}$ , which is perpendicular to the surface of the heterostructure. The maximal value of MR at  $7 \text{ T}$  ( $-7 \text{ T}$ ) is  $\sim 1.8\%$ . Different from parabolic ordinary MR curves, the typical weak antilocalization (WAL) feature, a cusp MR around  $B = 0$  (also shown in Figure S6), is clearly observed at the MR curves with the light power from  $0$  to  $15 \text{ mW}$ . The WAL effect originates from the quantum decoherence of the coherent electronic waves in the presence of spin relaxation related to Rashba spin-orbit coupling (SOC). To get a quantitative description of WAL, we performed a further analysis of the  $\Delta\sigma_{\text{WAL}} - B$  relation on the basis of the Maekawa-Fukuyama (MF) formula with a negligible Zeeman effect,<sup>47–49</sup>

$$\begin{aligned} \frac{\Delta\sigma(B)}{G_0} &= \frac{\Delta\sigma_{\text{WAL}}(B) + \Delta\sigma_{\text{OMR}}(B)}{G_0} \\ &= -\psi\left(\frac{1}{2} + \frac{B_{tr}}{B}\right) + \frac{3}{2}\psi\left(\frac{1}{2} + \frac{B_i + B_{so}}{B}\right) \\ &\quad - \frac{1}{2}\psi\left(\frac{1}{2} + \frac{B_i}{B}\right) - \ln\left(\frac{B_i + B_{so}}{B_{tr}}\right) \\ &\quad - \frac{1}{2}\ln\left(\frac{B_i + B_{so}}{B_i}\right) - A_k \frac{\sigma(0)}{G_0} \frac{B^2}{1 + CB^2} \end{aligned} \quad (2)$$

where  $\psi(x)$  is the digamma function defined as  $\psi(x) = \ln(x) + \psi\left(\frac{1}{2} + \frac{1}{x}\right)$  and  $B_{tr}$ ,  $B_i$  and  $B_{so}$  are the effective fields related to elastic scattering, inelastic scattering, and spin-orbit scattering, respectively. The  $\Delta\sigma$ , defined as  $\Delta\sigma = \sigma(B) - \sigma(0)$ , describes the total magneto-conductance including WAL induced quantum correction (first four terms) and ordinary magneto-conductance considering the orbital effect of magnetic field described by Kohler rule (the last term) here, and  $G_0 = e^2/\pi h$  is a universal value of conductance. As shown by the solid curves in Figure 5b, the experimental MR curves can be well fitted by the MF model. For the MR curve of  $P = 0 \text{ mW}$ , the negative slope at high field is characteristic of weak localization. All the curves were fitted only in the range  $0-3 \text{ T}$ . The values of parameters for each curve,  $B_{tr}$ ,  $B_i$  and  $B_{so}$ , can be obtained. The carrier density is a function of light power. Thus, the evolution of  $B_{tr}$ ,  $B_i$  and  $B_{so}$  as a function of carrier density is shown in Figure 5c. The carrier mobility depends on the elastic scattering of the conductive electrons at the interface of the heterostructure, so the dependence of the elastic scattering effective field ( $B_{tr}$ ) on the carrier density is related to that of the carrier mobility. The elastic scattering effective field is larger than the spin-orbit scattering effective field, and the inelastic scattering field is much less than the spin-orbit scattering effective field (Figure 5c), implying the dominant role of weak antilocalization. With the enhancement of the conductive carrier density, the spin-

orbit scattering effective field  $B_{so}$  also increases monotonously by 1 order of magnitude, from  $0.2$  to  $1.2 \text{ T}$ . The maximum of the  $B_{so}$  ( $1.2 \text{ T}$ ) is with the carrier density  $\sim 4 \times 10^{13} \text{ cm}^{-2}$ . The increase in  $B_{so}$  implies the enhancement of the strength of the spin-orbit coupling. The strength of the spin-orbit coupling is related to the carrier density (Fermi level), shown in the Supporting Information, Figure S6. Substantial enhancement of the spin-orbit coupling is demonstrated at the crossing region of the  $d_{xy}$  and  $d_{xz/yz}$  subbands, i.e., the Lifshitz transition point.<sup>8,31,50</sup> When the Fermi level is lower than the Lifshitz transition point, the spin-orbit coupling becomes stronger with the decrease in carrier density. According to Figures 4c and 5c, the linear Hall resistance curves and the disappearance of the peak value of  $B_{so}$  indicate that the saturation point of the carrier density under the light illumination is below the Lifshitz transition point.

The strength of spin-orbit coupling  $\alpha$  is a function of  $B_{so}$ , expressed as  $\alpha = \frac{\sqrt{eB_{so}}\hbar^3}{m^*}$ .<sup>51</sup> The spin-splitting energy  $\Delta$  is given by  $\Delta = 2k_F\alpha$ , in which  $k_F$  is the Fermi wave vector.  $k_F$  is calculated by  $k_F = \sqrt{2\pi n_s}$ , in which  $n_s$  is the carrier density. Figure 5d shows the deduced  $\alpha$  and  $\Delta$  as a function of the carrier density.  $\alpha$  and  $\Delta$  also grow monotonously from the initial values  $\sim 3.9 \times 10^{-12} \text{ eV m}$  and  $\sim 12 \text{ meV}$ , respectively. The maximum  $\alpha$  is  $\sim 9 \times 10^{-12} \text{ eV m}$ , while the maximum  $\Delta$  is  $\sim 29 \text{ meV}$ . The strength of spin-orbit coupling  $\alpha$  (Rashba coefficient) is close to that of the  $\text{AlO}_x/\text{KTO}$  heterostructure.<sup>52</sup> The spin-splitting energy is slightly higher than that of amorphous-LAO/KTO heterostructure.<sup>31</sup> Both the  $\alpha$  and  $\Delta$  are larger than those of STO-based 2DEG.<sup>6</sup> More importantly, the  $\alpha$  and  $\Delta$  are also higher than those of the (001) interface of YSZ/KTO heterostructure ( $\alpha \approx 5.5 \times 10^{-12} \text{ eV m}$ ,  $\Delta \approx 21 \text{ meV}$ ), another type of 5d 2DEG.<sup>53</sup>

As the maximum change of carrier density under the light is only  $\sim 3 \times 10^{12} \text{ cm}^{-2}$ , the strength of the spin-orbit coupling (Rashba coefficient) is modulated by  $\sim 5 \times 10^{-12} \text{ eV m}$ . The relative variation of  $\alpha$  is obviously larger than that of the amorphous-LAO/KTO heterostructure and STO-based 2DEG, where the change of  $n_s$  is on the order of magnitude of  $10^{13} \text{ cm}^{-2}$  with similar increments of  $\alpha$ .<sup>6,31</sup> This result indicates the unique characteristic of spin-orbit coupling for the CZO/KTO heterointerface. High-efficiency modulation of the strength of spin-orbit coupling can be achieved by light illumination. This phenomenon perhaps implies the unique band structure of the interface of the amorphous-CZO/KTO heterostructure.

#### 4. CONCLUSION

In conclusion, the  $\text{CaZrO}_3$  films were grown epitaxially on the KTO substrates. The crystallization quality of the CZO film decreased with the reduced deposition temperature. We obtained conductive interfaces at all deposition temperatures from  $700 \text{ }^\circ\text{C}$  to room temperature. With the decreasing deposition temperature, the critical thickness for the occurrence of the metallic interface increases from  $3.2$  to  $6 \text{ nm}$  at room temperature. The carrier density decreases with the reduced deposition temperature as the thickness of the CZO overlayer is fixed. Meanwhile, the conductive interface grown at room temperature shows the Kondo effect and the WAL effects derived from the spin-orbit coupling. The strength of spin-orbit coupling can be modulated by the light illumination with the carrier density changed. The maximum  $\alpha$

is  $\sim 9 \times 10^{-12}$  eV m with  $n_s \sim 4.2 \times 10^{13}$  cm $^{-2}$ . The strength of spin–orbit coupling goes up by  $\sim 5 \times 10^{-12}$  eV m, and it exhibits large relative variation as the carrier density only increases by  $3 \times 10^{12}$  cm $^{-2}$ . Our experiment provides an approach to designing on-demand properties of heterostructures with a conductive interface.

## ■ ASSOCIATED CONTENT

### SI Supporting Information

The Supporting Information is available free of charge at <https://pubs.acs.org/doi/10.1021/acsaelm.4c01618>.

AFM images of the surface of KTO substrate and CZO films, the XRR patterns for the measurement of CZO layer thickness, the XRD patterns of CZO/KTO and CZO/STO heterostructures prepared at different temperatures, the relation between electric transport characteristic and CZO layer thickness, and the dependence of spin–orbit coupling strength on the CZO layer thickness (PDF)

## ■ AUTHOR INFORMATION

### Corresponding Authors

**Yuansha Chen** – Beijing National Laboratory for Condensed Matter Physics and Institute of Physics, Chinese Academy of Sciences, Beijing 100190, People's Republic of China; University of Chinese Academy of Sciences, Beijing 100049, People's Republic of China; Email: [yschen@iphy.ac.cn](mailto:yschen@iphy.ac.cn)

**Yunzhong Chen** – Beijing National Laboratory for Condensed Matter Physics and Institute of Physics, Chinese Academy of Sciences, Beijing 100190, People's Republic of China; University of Chinese Academy of Sciences, Beijing 100049, People's Republic of China; [orcid.org/0000-0001-8368-5823](https://orcid.org/0000-0001-8368-5823); Email: [yzchen@iphy.ac.cn](mailto:yzchen@iphy.ac.cn)

**Jirong Sun** – Beijing National Laboratory for Condensed Matter Physics and Institute of Physics, Chinese Academy of Sciences, Beijing 100190, People's Republic of China; University of Chinese Academy of Sciences, Beijing 100049, People's Republic of China; [orcid.org/0000-0003-4531-4794](https://orcid.org/0000-0003-4531-4794); Email: [jrsun@iphy.ac.cn](mailto:jrsun@iphy.ac.cn)

### Authors

**Shaojin Qi** – School of Science, Shenyang University of Technology, Shenyang 110870, People's Republic of China; Beijing National Laboratory for Condensed Matter Physics and Institute of Physics, Chinese Academy of Sciences, Beijing 100190, People's Republic of China; University of Chinese Academy of Sciences, Beijing 100049, People's Republic of China; [orcid.org/0009-0000-5229-7174](https://orcid.org/0009-0000-5229-7174)

**Jiexing Liang** – School of Science, Shenyang University of Technology, Shenyang 110870, People's Republic of China

**Guimei Shi** – School of Science, Shenyang University of Technology, Shenyang 110870, People's Republic of China; [orcid.org/0000-0003-3936-9502](https://orcid.org/0000-0003-3936-9502)

**Yulin Gan** – Beijing National Laboratory for Condensed Matter Physics and Institute of Physics, Chinese Academy of Sciences, Beijing 100190, People's Republic of China; [orcid.org/0000-0003-0486-7026](https://orcid.org/0000-0003-0486-7026)

Complete contact information is available at: <https://pubs.acs.org/doi/10.1021/acsaelm.4c01618>

### Notes

The authors declare no competing financial interest.

## ■ ACKNOWLEDGMENTS

This work is supported by the National Key Research and Development Program of China (Grant Nos. 2021YFA1400300, 2023YFA1406400), the Science Center of the National Science Foundation of China (Grant No. 52088101), the National Basic Research of China (Grant Nos. 2022YFA1403302, 2023YFA1607400, 2019YFA0704904), the Project for Innovative Research Team of the National Natural Science Foundation of China (Project No. 11921004), the National Natural Science Foundation of China (Grant Nos. T2394472, 11934016, 51972335, 11704292, 12204523), the Strategic Priority Research Program (B) of the Chinese Academy of Sciences (No. XDB33030200), and 2024 Fundamental Research Project (No. LJ212410142016) of the Educational Department of Liaoning Province.

## ■ REFERENCES

- (1) Ohtomo, A.; Hwang, H. Y. A High-Mobility Electron Gas at the LaAlO<sub>3</sub>/SrTiO<sub>3</sub> Heterointerface. *Nature* **2004**, *427* (6973), 423–426.
- (2) Reyren, N.; Thiel, S.; Cavaglia, A. D.; Kourkoutis, L. F.; Hammerl, G.; Richter, C.; Schneider, C. W.; Kopp, T.; Rüetschi, A. S.; Jaccard, D.; Gabay, M.; Müller, D. A.; Triscone, J. M.; Mannhart, J. Superconducting Interfaces between Insulating Oxides. *Science* **2007**, *317* (5842), 1196–1199.
- (3) Brinkman, A.; Huijben, M.; Van Zalk, M.; Huijben, J.; Zeitler, U.; Maan, J. C.; Van der Wiel, W. G.; Rijnders, G.; Blank, D. H. A.; Hilgenkamp, H. Magnetic Effects at the Interface between Non-Magnetic Oxides. *Nat. Mater.* **2007**, *6* (7), 493–496.
- (4) Moetakef, P.; Zhang, J. Y.; Kozhanov, A.; Jalan, B.; Seshadri, R.; Allen, S. J.; Stemmer, S. Transport in Ferromagnetic GdTiO<sub>3</sub>/SrTiO<sub>3</sub> Heterostructures. *Appl. Phys. Lett.* **2011**, *98* (11), No. 112110.
- (5) Niu, W.; Wang, X. F.; Xu, Y. B.; Zhang, R. Recent Advances on Spin-Polarized Two-Dimensional Electron Gases at Oxide Interfaces. *ACS Appl. Electron. Mater.* **2021**, *3* (1), 128–144.
- (6) Cavaglia, A. D.; Gabay, M.; Gariglio, S.; Reyren, N.; Cancellieri, C.; Triscone, J. M. Tunable Rashba Spin-Orbit Interaction at Oxide Interfaces. *Phys. Rev. Lett.* **2010**, *104* (12), No. 126803.
- (7) Yang, R. S.; Yin, H.; Li, M.; Wang, S. H.; Jin, K. X. Manipulating Spin-Orbit Coupling at Oxide Interfaces by Lanthanum Cobaltate. *ACS Appl. Electron. Mater.* **2022**, *4* (3), 1117–1123.
- (8) Cheng, L.; Wei, L.; Liang, H.; Yan, Y.; Cheng, G.; Lv, M.; Lin, T.; Kang, T.; Yu, G.; Chu, J.; Zhang, Z.; Zeng, C. Optical Manipulation of Rashba Spin–Orbit Coupling at SrTiO<sub>3</sub>-Based Oxide Interfaces. *Nano Lett.* **2017**, *17* (11), 6534–6539.
- (9) Li, M.; Ding, Z. Y.; Li, L. Y.; Liu, Y. Q.; Yang, S. W.; Wu, G.; Yang, X. P. Tunable 5d-t<sub>2g</sub> Mott State and Monoatomic Layer Two-Dimensional Electron Gas Realized in Spin-Orbit-Coupled SrIrO<sub>3</sub> through Heterostructuring. *ACS Appl. Electron. Mater.* **2024**, *6* (8), 6155–6164.
- (10) Wang, Y.; Ramaswamy, R.; Motapothula, M.; Narayanapillai, K.; Zhu, D. P.; Yu, J. W.; Venkatesan, T.; Yang, H. S. Room-Temperature Giant Charge-to-Spin Conversion at the SrTiO<sub>3</sub>–LaAlO<sub>3</sub> Oxide Interface. *Nano Lett.* **2017**, *17* (12), 7659–7664.
- (11) Lesne, E.; Fu, Y.; Oyarzun, S.; Rojas-Sanchez, J. C.; Vaz, D. C.; Naganuma, H.; Sicoli, G.; Attane, J. P.; Jamet, M.; Jacquet, E.; George, J. M.; Barthelemy, A.; Jaffres, H.; Fert, A.; Bibes, M.; Vila, L. Highly Efficient and Tunable Spin-to-Charge Conversion through Rashba Coupling at Oxide Interfaces. *Nat. Mater.* **2016**, *15* (12), 1261–1266.
- (12) Ohtomo, A.; Müller, D. A.; Grazul, J. L.; Hwang, H. Y. Artificial charge-modulation in atomic-scale perovskite titanate superlattices. *Nature* **2002**, *419* (6905), 378–380.
- (13) Gunkel, F.; Skaja, K.; Shkabko, A.; Dittmann, R.; Hoffmann-Eifert, S.; Waser, R. Stoichiometry Dependence and Thermal Stability of Conducting NdGaO<sub>3</sub>/SrTiO<sub>3</sub> Heterointerfaces. *Appl. Phys. Lett.* **2013**, *102* (7), No. 071601.

- (14) Gunkel, F.; Bell, C.; Inoue, H.; Kim, B.; Swartz, A. G.; Merz, T. A.; Hikita, Y.; Harashima, S.; Sato, H. K.; Minohara, M.; Hoffmann-Eifert, S.; Dittmann, R.; Hwang, H. Y. Defect Control of Conventional and Anomalous Electron Transport at Complex Oxide Interfaces. *Phys. Rev. X* **2016**, *6* (3), No. 031035.
- (15) Chen, Y. Z.; Bovet, N.; Trier, F.; Christensen, D. V.; Qu, F. M.; Andersen, N. H.; Kasama, T.; Zhang, W.; Giraud, R.; Dufouleur, J.; Jespersen, T. S.; Sun, J. R.; Mith, A.; Nygard, J.; Lu, L.; Buechner, B.; Shen, B. G.; Linderoth, S.; Pryds, N. A High-Mobility Two-Dimensional Electron Gas at the Spinel/Perovskite Interface of Gamma-Al<sub>2</sub>O<sub>3</sub>/SrTiO<sub>3</sub>. *Nat. Commun.* **2013**, *4*, 1371.
- (16) Chen, Y. Z.; Bovet, N.; Kasama, T.; Gao, W. W.; Yazdi, S.; Ma, C.; Pryds, N.; Linderoth, S. Room Temperature Formation of High-Mobility Two-Dimensional Electron Gases at Crystalline Complex Oxide Interfaces. *Adv. Mater.* **2014**, *26* (9), 1462.
- (17) Chen, Y. Z.; Trier, F.; Kasama, T.; Christensen, D. V.; Bovet, N.; Balogh, Z. I.; Li, H.; Thyden, K. T. S.; Zhang, W.; Yazdi, S.; Norby, P.; Pryds, N.; Linderoth, S. Creation of High Mobility Two-Dimensional Electron Gases via Strain Induced Polarization at an Otherwise Nonpolar Complex Oxide Interface. *Nano Lett.* **2015**, *15* (3), 1849–1854.
- (18) Niu, W.; Chen, Y. D.; Gan, Y. L.; Zhang, Y.; Zhang, X. Q.; Yuan, X.; Cao, Z.; Liu, W. Q.; Xu, Y. B.; Zhang, R.; Pryds, N.; Chen, Y. Z.; Pu, Y.; Wang, X. F. Electrolyte gate controlled metal-insulator transitions of the CaZrO<sub>3</sub>/SrTiO<sub>3</sub> heterointerface. *Appl. Phys. Lett.* **2019**, *115* (6), No. 061601.
- (19) Hwang, H. Y.; Iwasa, Y.; Kawasaki, M.; Keimer, B.; Nagaosa, N.; Tokura, Y. Emergent phenomena at oxide interfaces. *Nat. Mater.* **2012**, *11* (2), 103–113.
- (20) Nakagawa, N.; Hwang, H. Y.; Muller, D. A. Why some interfaces cannot be sharp. *Nat. Mater.* **2006**, *5* (3), 204–209.
- (21) Chen, Y. Z.; Pryds, N.; Kleibeuker, J. E.; Koster, G.; Sun, J. R.; Stamate, E.; Shen, B. G.; Rijnders, G.; Linderoth, S. Metallic and Insulating Interfaces of Amorphous SrTiO<sub>3</sub>-Based Oxide Heterostructures. *Nano Lett.* **2011**, *11* (9), 3774–3778.
- (22) Chen, Y. Z.; Christensen, D. V.; Trier, F.; Pryds, N.; Smith, A.; Linderoth, S. On the origin of metallic conductivity at the interface of LaAlO<sub>3</sub>/SrTiO<sub>3</sub>. *Appl. Surf. Sci.* **2012**, *258* (23), 9242–9245.
- (23) Ding, J. F.; Cheng, J. L.; Dogan, F.; Li, Y. Y.; Lin, W. N.; Yao, Y. B.; Manchon, A.; Yang, K. S.; Wu, T. Two-Dimensional Electron Gas at the Spinel/Perovskite Interface: Suppression of Polar Catastrophe by an Ultrathin Layer of Interfacial Defects. *ACS Appl. Mater. Interfaces* **2020**, *12* (38), 42982–42991.
- (24) Harashima, S.; Bell, C.; Kim, M.; Yajima, T.; Hikita, Y.; Hwang, H. Y. Coexistence of two-dimensional and three-dimensional Shubnikov–de Haas oscillations in Ar-irradiated KTaO<sub>3</sub>. *Phys. Rev. B* **2013**, *88* (8), No. 085102.
- (25) Höchli, U. T.; Weibel, H. E.; Boatner, L. A. Quantum Limit of Ferroelectric Phase Transitions in KTa<sub>1-x</sub>Nb<sub>x</sub>O<sub>3</sub>. *Phys. Rev. Lett.* **1977**, *39* (18), 1158.
- (26) Zhang, H. R.; Yun, Y.; Zhang, X. J.; Zhang, H.; Ma, Y.; Yan, X.; Wang, F.; Li, G.; Li, R.; Khan, T.; Chen, Y. S.; Liu, W.; Hu, F. X.; Liu, B. G.; Shen, B. G.; Han, W.; Sun, J. R. High-Mobility Spin-Polarized Two-Dimensional Electron Gases at EuO/KTaO<sub>3</sub> Interfaces. *Phys. Rev. Lett.* **2018**, *121* (11), No. 116803.
- (27) Liu, C. J.; Yan, X.; Jin, D. F.; Ma, Y.; Hsiao, H. W.; Lin, Y. L.; Bretz-Sullivan, T. M.; Zhou, X. J.; Pearson, J.; Fisher, B.; Jiang, J. S.; Han, W.; Zuo, J. M.; Wen, J. G.; Fong, D. D.; Sun, J. R.; Zhou, H.; Bhattacharya, A. Two-dimensional superconductivity and anisotropic transport at KTaO<sub>3</sub> (111) interfaces. *Science* **2021**, *371* (6530), 716–721.
- (28) Chen, Z.; Liu, Z. R.; Sun, Y. Q.; Chen, X. X.; Liu, Y.; Zhang, H.; Li, H. K.; Zhang, M.; Hong, S. Y.; Ren, T. S.; Zhang, C.; Tian, H.; Zhou, Y.; Sun, J. R.; Xie, Y. W. Two-Dimensional Superconductivity at the LaAlO<sub>3</sub>/KTaO<sub>3</sub>(110) Heterointerface. *Phys. Rev. Lett.* **2021**, *126* (2), No. 026802.
- (29) Hua, X. Y.; Meng, F. B.; Huang, Z. Y.; Li, Z. H.; Wang, S.; Ge, B. H.; Xiang, Z. J.; Chen, X. H. Tunable two-dimensional superconductivity and spin-orbit coupling at the EuO/KTaO<sub>3</sub>(110) interface. *npj Quantum Mater.* **2022**, *7* (1), 97.
- (30) Chen, Z.; Liu, Y.; Zhang, H.; Liu, Z. R.; Tian, H.; Sun, Y. Q.; Zhang, M.; Zhou, Y.; Sun, J. R.; Xie, Y. W. Electric field control of superconductivity at the LaAlO<sub>3</sub>/KTaO<sub>3</sub>(111) interface. *Science* **2021**, *372* (6543), 721–724.
- (31) Zhang, H.; Yan, X.; Zhang, X. J.; Wang, S.; Xiong, C. M.; Zhang, H. R.; Qi, S. J.; Zhang, J. E.; Han, F. R.; Wu, N.; Liu, B. G.; Chen, Y. S.; Shen, B. G.; Sun, J. R. Unusual Electric and Optical Tuning to KTaO<sub>3</sub>-Based Two-Dimensional Electron Gases with 5d orbitals. *ACS Nano* **2019**, *13* (1), 609–615.
- (32) Gan, Y. L.; Yang, F. Z.; Kong, L. Y.; Chen, X. J.; Xu, H.; Zhao, J.; Li, G.; Zhao, Y. C.; Yan, L.; Zhong, Z. C.; Chen, Y. Z.; Ding, H. Light-Induced Giant Rashba Spin-Orbit Coupling at Superconducting KTaO<sub>3</sub>(110) Heterointerfaces. *Adv. Mater.* **2023**, *35* (25), No. 2300582.
- (33) Zhang, H.; Yan, X.; Zhang, J.; Zhang, J. E.; Han, F. R.; Huang, H. L.; Qi, S. J.; Shi, W. X.; Shen, B. G.; Sun, J. R. The effect of fabrication conditions on 2DEGs transport characteristics at amorphous-LaAlO<sub>3</sub>/KTaO<sub>3</sub> interfaces. *Mater. Res. Express* **2019**, *6* (8), No. 086448.
- (34) Zhang, H.; Zhang, H. R.; Yan, X.; Zhang, X. J.; Zhang, Q. H.; Zhang, J.; Han, F. R.; Gu, L.; Liu, B. G.; Chen, Y. S.; Shen, B. G.; Sun, J. R. Highly Mobile Two-Dimensional Electron Gases with a Strong Gating Effect at the Amorphous LaAlO<sub>3</sub>/KTaO<sub>3</sub> Interface. *ACS Appl. Mater. Interfaces* **2017**, *9* (41), 36456–36461.
- (35) Zou, K.; Ismail-Beigi, S.; Kisslinger, K.; Shen, X.; Su, D.; Walker, F. J.; Ahn, C. H. LaTiO<sub>3</sub>/KTaO<sub>3</sub> interfaces: A new two dimensional electron gas system. *APL Mater.* **2015**, *3* (3), No. 036104.
- (36) Zou, Y. T.; Shin, H.; Wei, H. R.; Fan, Y. Y.; Davidson, B. A.; Guo, E. J.; Chen, Q. H.; Zou, K.; Cheng, Z. G. Transport behaviors of topological band conduction in KTaO<sub>3</sub>'s two-dimensional electron gases. *npj Quantum Mater.* **2022**, *7* (1), 122.
- (37) Xu, H.; Gan, Y. L.; Zhao, Y. C.; Li, M. H.; Hu, X. Z.; Chen, X. Z.; Wang, R. W.; Li, Y.; Sun, J. R.; Hu, F. X.; Chen, Y. Z.; Shen, B. G. Two-Dimensional Electron Gases at the Amorphous and Crystalline SrTiO<sub>3</sub>/KTaO<sub>3</sub> Heterointerfaces. *Phys. Status Solidi A* **2023**, *220* (13), No. 2300235.
- (38) Goyal, S.; Wadehra, N.; Chakraverty, S. Tuning the Electrical State of 2DEG at LaVO<sub>3</sub>/KTaO<sub>3</sub> Interface: Effect of Light and Electrostatic Gate. *Adv. Mater. Interfaces* **2020**, *7* (16), No. 2000646.
- (39) Wadehra, N.; Tomar, R.; Varma, R. M.; Gopal, R. M.; Singh, Y.; Dattagupta, S.; Chakraverty, S. Planar Hall effect and anisotropic magnetoresistance in polar-polar interface of LaVO<sub>3</sub>-KTaO<sub>3</sub> with strong spin-orbit coupling. *Nat. Commun.* **2020**, *11* (1), 874.
- (40) Al-Tawhid, A. H.; Kumah, D. P.; Ahadi, K. Two-dimensional electron systems and interfacial coupling in LaCrO<sub>3</sub>/KTaO<sub>3</sub> heterostructures. *Appl. Phys. Lett.* **2021**, *118* (19), No. 192905.
- (41) Qi, S. J.; Zhang, H.; Zhang, J. E.; Gan, Y. L.; Chen, X. B.; Shen, B. G.; Chen, Y. S.; Chen, Y. Z.; Sun, J. R. Large Optical Tunability of 5d 2D Electron Gas at the Spinel/Perovskite  $\gamma$ -Al<sub>2</sub>O<sub>3</sub>/KTaO<sub>3</sub> Heterointerface. *Adv. Mater. Interfaces* **2022**, *9* (20), No. 2200103.
- (42) Zhang, X.; Zhu, T. S.; Zhang, S.; Chen, Z. Q.; Song, A.; Zhang, C.; Gao, R. Z.; Niu, W.; Chen, Y. Q.; Fei, F. C.; Tai, Y. L.; Li, G.; Ge, B. H.; Lou, W. K.; Shen, J.; Zhang, H. J.; Chang, K.; Song, F. Q.; Zhang, R.; Wang, X. F. Light-induced giant enhancement of nonreciprocal transport at KTaO<sub>3</sub>-based interfaces. *Nat. Commun.* **2024**, *15* (1), 2992.
- (43) Mathews, M. D.; Mirza, E. B.; Momin, A. C. High-temperature X-ray diffractometric studies of CaZrO<sub>3</sub>, SrZrO<sub>3</sub> and BaZrO<sub>3</sub>. *J. Mater. Sci. Lett.* **1991**, *10* (6), 305–306.
- (44) Hamann, D. R. New Solution for Exchange Scattering in Dilute Alloys. *Phys. Rev.* **1967**, *158* (3), 570–580.
- (45) Wadehra, N.; Tomar, R.; Halder, S.; Sharma, M.; Singh, I.; Jena, N.; Prakash, B.; De Sarkar, A.; Bera, C.; Venkatesan, A.; Chakraverty, S. Electronic structure modification of the KTaO<sub>3</sub> single-crystal surface by Ar<sup>+</sup> bombardment. *Phys. Rev. B* **2017**, *96* (11), No. 115423.

(46) Liu, G. Z.; Qiu, J.; Jiang, Y. C.; Zhao, R.; Yao, J. L.; Zhao, M.; Feng, Y.; Gao, J. Light induced suppression of Kondo effect at amorphous LaAlO<sub>3</sub>/SrTiO<sub>3</sub> interface. *Appl. Phys. Lett.* **2016**, *109* (3), No. 031110.

(47) Maekawa, S.; Fukuyama, H. Magnetoresistance in two-dimensional disordered systems: effects of Zeeman splitting and spin-orbit scattering. *J. Phys. Soc. Jpn.* **1981**, *50* (8), 2516–2524.

(48) Yin, H.; Wang, S. H.; Jin, K. X. Enhanced Rashba Spin Orbit Coupling and Magnetic Behavior at Oxide Heterointerfaces by Optical Gating. *J. Phys. Chem. Lett.* **2023**, *14* (38), 8684–8690.

(49) Herranz, G.; Singh, G.; Bergeal, N.; Jouan, A.; Lesueur, J.; Gazquez, J.; Varela, M.; Scigaj, M.; Dix, N.; Sanchez, F.; Fontcuberta, J. Engineering Two-Dimensional Superconductivity and Rashba Spin-Orbit Coupling in LaAlO<sub>3</sub>/SrTiO<sub>3</sub> Quantum Wells by Selective Orbital Occupancy. *Nat. Commun.* **2015**, *6*, 6028.

(50) Joshua, A.; Pecker, S.; Ruhman, J.; Altman, E.; Ilani, S. A universal critical density underlying the physics of electrons at the LaAlO<sub>3</sub>/SrTiO<sub>3</sub> interface. *Nat. Commun.* **2012**, *3*, 1129.

(51) Gopinadhan, K.; Annadi, A.; Kim, Y.; Srivastava, A.; Kumar, B.; Chen, J. S.; Coey, J. M. D.; Ariando; Venkatesan, T. Gate Tunable In- and Out-of-Plane Spin–Orbit Coupling and Spin-Splitting Anisotropy at LaAlO<sub>3</sub>/SrTiO<sub>3</sub>(110) Interface. *Adv. Electron. Mater.* **2015**, *1* (8), No. 1500114.

(52) Vicente-Arche, L. M.; Brehin, J.; Varotto, S.; Cosset-Cheneau, M.; Mallik, S.; Salazar, R.; Noel, P.; Vaz, D. C.; Trier, F.; Bhattacharya, S.; Sander, A.; Menard, G.; Bergeal, N.; Barthelemy, A.; Li, H.; Lin, C. C.; Barthelemy, D. E.; Young, I. A.; Rault, J. E.; Vila, L.; Attane, J. P.; Bibes, M. Spin–Charge Interconversion in KTaO<sub>3</sub> 2D Electron Gases. *Adv. Mater.* **2021**, *33* (43), No. 2102102.

(53) Xu, H.; Li, H.; Gauquelin, N.; Chen, X. J.; Wu, W. F.; Zhao, Y. C.; Si, L.; Tian, D.; Li, L.; Gan, Y. L.; Qi, S. J.; Li, M. H.; Hu, F. X.; Sun, J. R.; Jannis, D.; Yu, P.; Chen, G.; Zhong, Z. C.; Radovic, M.; Verbeeck, J.; Chen, Y. Z.; Shen, B. G. Giant Tunability of Rashba Splitting at Cation-Exchanged Polar Oxide Interfaces by Selective Orbital Hybridization. *Adv. Mater.* **2024**, *36* (29), No. 2313297.